

Accurate Thickness Measurement of Two Adjacent Sheet Structures in CT Images

Yuanzhi CHENG^{†,††}, Nonmember, Yoshinobu SATO^{†a)}, Member, Hisashi TANAKA[†], Takashi NISHII[†], Nobuhiko SUGANO[†], Hironobu NAKAMURA[†], Hideki YOSHIKAWA[†], Shuguo WANG^{††}, Nonmembers, and Shinichi TAMURA[†], Member

SUMMARY Accurate thickness measurement of sheet-like structure such as articular cartilage in CT images is required in clinical diagnosis as well as in fundamental research. Using a conventional measurement method based on the zero-crossing edge detection (zero-crossings method), several studies have already analyzed the accuracy limitation on thickness measurement of the single sheet structure that is not influenced by peripheral structures. However, no studies, as of yet, have assessed measurement accuracy of two adjacent sheet structures such as femoral and acetabular cartilages in the hip joint. In this paper, we present a model of the CT scanning process of two parallel sheet structures separated by a small distance, and use the model to predict the shape of the gray-level profiles along the sheet normal orientation. The difference between the predicted and the actual gray-level profiles observed in the CT data is minimized by refining the model parameters. Both a one-by-one search (exhaustive combination search) technique and a nonlinear optimization technique based on the Levenberg-Marquardt algorithm are used to minimize the difference. Using CT images of phantoms, we present results showing that when applying the one-by-one search method to obtain the initial values of the model parameters, Levenberg-Marquardt method is more accurate than zero-crossings and one-by-one search methods for estimating the thickness of two adjacent sheet structures, as well as the thickness of a single sheet structure.

key words: cartilage thickness, hip joint, image quantification, numerical simulation, point spread function

1. Introduction

Accurate thickness measurement of sheet-like structure such as articular cartilage has become increasingly important in clinical applications as well as in fundamental research. A number of studies for measuring articular cartilage thickness have been performed. Most of them have reported on the knee joint cartilage [1]–[5], only a few of them investigate the hip joint cartilage [6], [7].

Although several studies [8], [9] have already analyzed the accuracy limitation on thickness measurement of sheet structures by using the conventional techniques based on the zero-crossing edge detection (zero-crossings method), these results are valid under the restriction that the sheet structure is not influenced by its peripheral structures. In such cases, we call this sheet structure “single sheet structure”. The sheet structures in the actual medical images often violate the restriction. For example, the femoral cartilage of the

hip joint is close to the acetabular cartilage. In this case, two cartilages (two sheet structures) may influence each other. To our knowledge, no studies, as of yet, have assessed this influence.

In this paper, we present a model of the CT scanning process of two adjacent sheet structures separated by a small distance for measuring the thickness of sheet structures. Using this model, we can predict the shape of the gray-level profile along the normal orientation of the sheet surface. We demonstrate that the zero-crossings method can introduce large measurement errors in thickness measurement. In our proposed approach, the estimation problem is formulated as a least square fitting of an actual gray-level profile observed in the CT data set to a predicted gray-level profile. The difference between the predicted and the actual gray-level profiles observed in the CT data is minimized by refining the model parameters. Both a one-by-one search (exhaustive combination search) technique and a nonlinear optimization technique based on the Levenberg-Marquardt algorithm are used to minimize the difference between predicted and actual gray-level profiles. The set of parameters that minimizes the difference between the model and the actual image yields the thickness estimation of the sheet structure. Using CT images of phantoms, we compare the performance of three methods (zero-crossings, one-by-one search, and Levenberg-Marquardt).

2. Methods and Materials

2.1 Modeling Two Adjacent Sheet Structures

Assuming that $Sheet_1$ and $Sheet_2$ represent the three-dimensional (3D) two adjacent and parallel sheet structures, which model the both cartilages in the hip joint. Let us consider the sheet structure is oriented obliquely to the scan plane of CT imaging at an angle θ (Fig. 1). The 3D two sheet structures perpendicular to the x axis, can be modeled as

$$s_0(\vec{x}; \tau_1, \tau_0, \tau_2) = g(x; \tau_1, \tau_0, \tau_2), \quad (1)$$

where $\vec{x} = (x, y, z)^T$, and

$$g(x; \tau_1, \tau_0, \tau_2) = \begin{cases} H_b, & x < -\tau_1 - \tau_0/2 \\ H_t, & -\tau_1 - \tau_0/2 \leq x \leq -\tau_0/2 \\ H_0, & -\tau_0/2 < x < \tau_0/2 \\ H_t, & \tau_0/2 \leq x \leq \tau_0/2 + \tau_2 \\ H_b, & x > \tau_0/2 + \tau_2 \end{cases} \quad (2)$$

Manuscript received April 05, 2006.

Manuscript revised July 19, 2006.

[†]The authors are with the Division of Image Analysis, Osaka University Graduate School of Medicine, Suita-shi, 565-0871 Japan.

^{††}The authors are with Robot Research Institute, Harbin Institute of Technology, China.

a) E-mail: yoshi@image.med.osaka-u.ac.jp

DOI: 10.1093/ietisy/e90-d.1.271

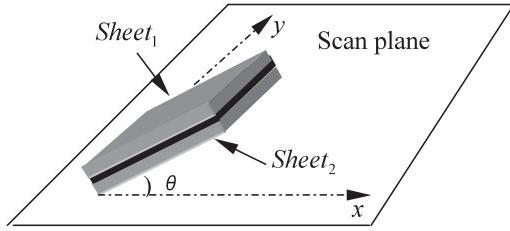


Fig. 1 Ideal model of two adjacent sheet structures separated by a small distance, which models the two cartilages in the hip joint. Let *Sheet₁* and *Sheet₂* represent the left and right side structures. The sheet structure is oriented obliquely to the scan plane at an angle θ .

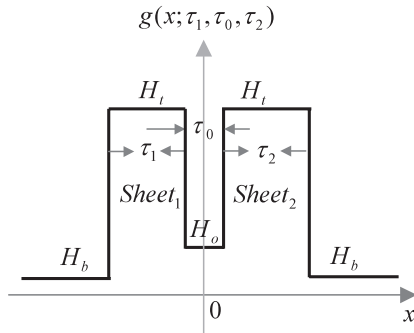


Fig. 2 1D profile of ideal density distributions along the normal orientation of sheet surface for two adjacent sheets. τ_1 , τ_2 , and τ_0 are *Sheet₁* thickness, *Sheet₂* thickness, and distance between them, respectively. H_b , H_t , and H_0 denote the ideal density heights of the background of both sides, the two adjacent sheets, and the space between them, respectively.

in which τ_1 , τ_2 , and τ_0 represent *Sheet₁* thickness, *Sheet₂* thickness, and distance between them, respectively. H_b , H_t , and H_0 denote the ideal density heights of the background of both sides, the two adjacent sheets, and the space between them, respectively (Fig. 2). Two adjacent sheets with rotation θ around the y axis can be written as

$$s(\vec{x}; \tau_1, \tau_0, \tau_2, \theta) = s_0(\vec{x}'; \tau_1, \tau_0, \tau_2), \quad (3)$$

where $\vec{x}' = R_\theta \vec{x}$, in which R_θ denotes 3×3 matrix representing rotation θ around the y axis.

2.2 Modeling CT Imaging

If the imaging system is linear, the image of an object can be expressed as the linear convolution of an object with the PSF (point spread function) of the imaging system. For the CT scanner, the scanning process can be modeled as a linear convolution of the object with the PSF of the CT system [9], [10]. The CT scanner PSF represents the resolution-limiting factors that cause images not to be replicas of the real objects. An ideal PSF is an impulse, and any deviation from this ideal function cause the PSF to widen. The increase in PSF width increase the blur that images incur as a result of being generated by this nonideal system. The spatial resolution of CT scanner system can be characterized by its 3D PSF. The 3D PSF is modeled as a Gaussian function [10], [11], $Gauss(\vec{x}; \sigma_x, \sigma_y, \sigma_z)$, which is given by

$$\begin{aligned} psf(\vec{x}) &= Gauss(\vec{x}; \sigma_x, \sigma_y, \sigma_z) \\ &= \frac{1}{2\pi^{\frac{3}{2}} \sigma_x \sigma_y \sigma_z} e^{-\left(\frac{x^2}{2\sigma_x^2} + \frac{y^2}{2\sigma_y^2} + \frac{z^2}{2\sigma_z^2}\right)}, \end{aligned} \quad (4)$$

where $psf(\vec{x})$ is the 3D PSF of the scanner, and σ_x , σ_y , and σ_z are the standard deviations in the x , y , and z directions, respectively. We assume that the parameters σ_x , σ_y , and σ_z are estimated beforehand by a calibration procedure. The estimation procedures for the PSF of the scanner are described later in Sect. 2.5.

The scanning process is modeled as the 3D linear convolution of the 3D two adjacent sheets with the 3D ideal scanner model [9], [10] and written as

$$f(\vec{x}; \tau_1, \tau_0, \tau_2) = s(\vec{x}; \tau_1, \tau_0, \tau_2, \theta) * psf(\vec{x}), \quad (5)$$

where $s(\vec{x}; \tau_1, \tau_0, \tau_2, \theta)$ is the 3D ideal two adjacent structures with rotation θ , $*$ denotes the convolution operation, $psf(\vec{x})$ is the 3D PSF of the scanner, and $f(\vec{x}; \tau_1, \tau_0, \tau_2)$ is the resultant 3D blurred image. The 1D profiles of $f(\vec{x}; \tau_1, \tau_0, \tau_2)$ along the straight line are given by

$$\vec{x} = s \cdot \vec{r}_\theta, \quad (6)$$

where s is a parameter representing the position on the sheet normal direction $\vec{r}_\theta = (-\sin \theta, 0, \cos \theta)$. Thus, by substituting Eq. (6) for \vec{x} in $f(\vec{x}; \tau_1, \tau_0, \tau_2)$, the simulated gray-level (scanner responses) along the line can be written as

$$f(s; \tau_1, \tau_0, \tau_2) = f(s \cdot \vec{r}_\theta; \tau_1, \tau_0, \tau_2, \vec{r}_\theta). \quad (7)$$

Figure 3 shows the density profiles of ideal model and simulated scanner responses along \vec{r}_θ for two adjacent sheets (Fig. 3 (a)) and a single sheet (Fig. 3 (b)). Comparing Fig. 3 (a) with Fig. 3 (b), it can be seen that the scanner responses of *Sheet₂* were influenced by *Sheet₁*.

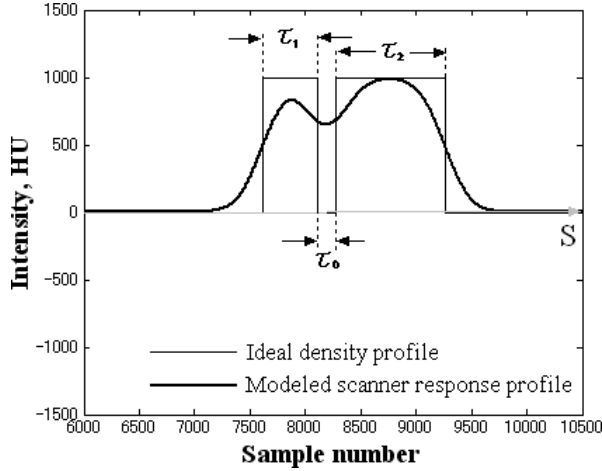
2.3 Numerical Simulation Analysis of Zero-Crossings Method

To illustrate the potential measurement errors when applying the zero-crossings method for two adjacent sheets, we measure the thickness of *Sheet₂* using the zero-crossings method. Measured thickness is defined as the shortest distance between the left and right sides of the edges of sheet structure, which are the zero-crossings of second directional derivatives combined with Gaussian blurring along the normal orientation of the sheet surface. In actual situations, Gaussian blurring is employed to reduce the effect of noise.

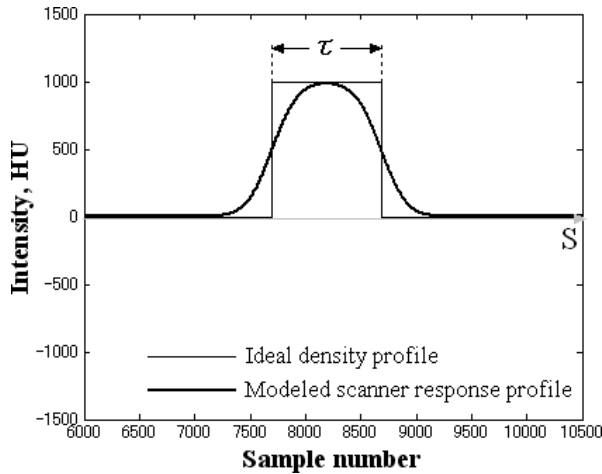
When the Gaussian filter is applied to the acquired 3D data by post-processing, the Gaussian filtered 3D data of the sheet structure is given by

$$f(\vec{x}; \tau_1, \tau_0, \tau_2, \sigma_f) = f(\vec{x}; \tau_1, \tau_0, \tau_2) * Gauss(\vec{x}; \sigma_f), \quad (8)$$

where σ_f is the filter width. Thickness measurement of sheet structures can be performed only through analyzing 1D profiles of the second directional derivative $f''(\vec{x}; \tau_1, \tau_0, \tau_2, \sigma_f, \vec{r}_\theta)$ and the first directional derivative $f'(\vec{x}; \tau_1, \tau_0, \tau_2, \sigma_f, \vec{r}_\theta)$ of 3D data $f(\vec{x}; \tau_1, \tau_0, \tau_2, \sigma_f)$ along



(a)



(b)

Fig. 3 Simulated scanner responses along the sheet normal direction. The sheet structure is oriented obliquely to the scan plane at an angle $\theta = 30^\circ$, and the scanner PSF parameters are $\sigma_x = \sigma_y = \sigma_{xy} = 0.45$ and $\sigma_z = 0.55$, respectively. (a) Two adjacent sheets with $\tau_1 = 1.5$ mm, $\tau_0 = 0.5$ mm, and $\tau_2 = \tau = 3.0$ mm. (b) Single sheet with a thickness of $\tau = 3.0$ mm. Note that despite of $\tau_2 = \tau = 3.0$ mm, gray-level profile of *Sheet*₂ is different from that of single sheet because *Sheet*₁ and *Sheet*₂ influence each other.

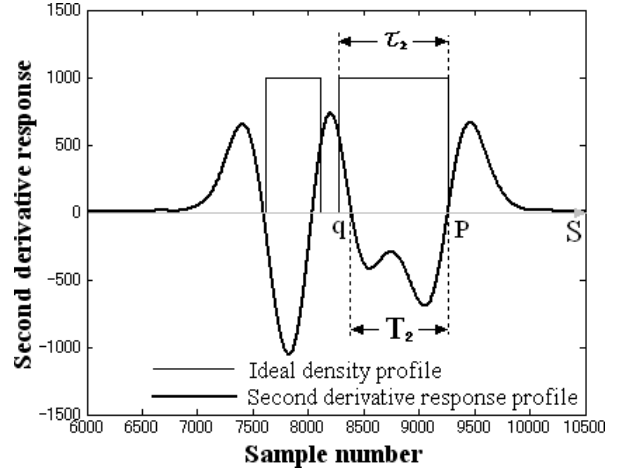
the sheet normal direction \vec{r}_θ , where $\vec{r}_\theta = (-\sin \theta, 0, \cos \theta)$ (see [8] for the procedures of obtaining $f''(\vec{x}; \tau_1, \tau_0, \tau_2, \sigma_f, \vec{r}_\theta)$ and $f'(\vec{x}; \tau_1, \tau_0, \tau_2, \sigma_f, \vec{r}_\theta)$). By substituting Eq. (6) for \vec{x} in $f''(\vec{x}; \tau_1, \tau_0, \tau_2, \sigma_f, \vec{r}_\theta)$, the second directional derivative along the line can be written as

$$f''(s) = f''(s \cdot \vec{r}_\theta; \tau_1, \tau_0, \tau_2, \sigma_f, \vec{r}_\theta). \quad (9)$$

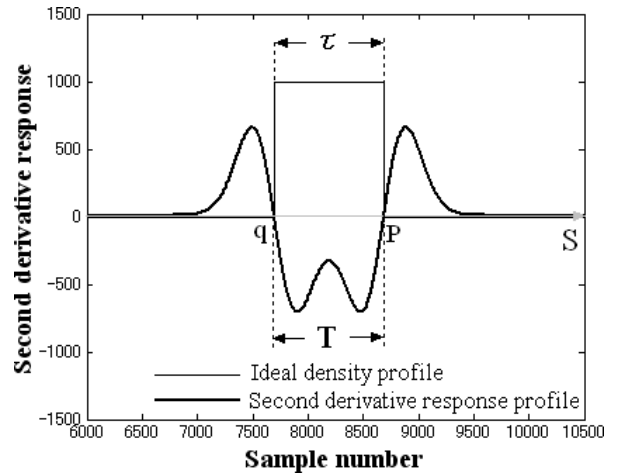
Similarly, the first directional derivative along the line can be written as

$$f'(s) = f'(s \cdot \vec{r}; \tau_1, \tau_0, \tau_2, \sigma_f, \vec{r}_\theta). \quad (10)$$

Figure 4(a) illustrates how thickness of *Sheet*₂ is determined by using a zero-crossings method along the sheet normal orientation. We get zero-crossing points $s = q$ and $s = p$ on the left and right sides of the edges for *Sheet*₂, which satisfy $f''(s) = 0$. Let zero-crossing points q and p



(a)



(b)

Fig. 4 Measured thickness of the sheet structures by using zero-crossings method. The tilt angle $\theta = 30^\circ$; the in-plane scanner PSF: $\sigma_x = \sigma_y = \sigma_{xy} = 0.45$ and the scanner PSF in the z direction: $\sigma_z = 0.55$; Gaussian filter width $\sigma_f = 0.25$ mm for zero-crossings method. $\tau_1 = 1.5$ mm, $\tau_0 = 0.5$ mm, $\tau_2 = \tau = 3.0$ mm. (a) Two adjacent sheets. Measured thickness of *Sheet*₂: $T_2 = |p - q|$. In the case of $\tau_0 = 0.5$ mm, thickness of $\tau_2 = 3.0$ mm was measured by approximately 2.63 mm (−12.3% error). (b) Single sheet. Measured thickness: $T = |p - q|$. Thickness of $\tau = 3.0$ mm was measured by approximately 3.03 mm (1% error). Compared with a single sheet, thickness of *Sheet*₂ was underestimated.

correspond to the minimum and maximum values of $f'(s)$ among those satisfying the condition given by $f''(s) = 0$. The measured thickness, T_2 , of *Sheet*₂ is defined as the distance between p and q , as follows

$$T_2 = |p - q|. \quad (11)$$

In Fig. 4(a), with $\tau_1 = 1.5$ mm, $\tau_0 = 0.5$ mm, $\tau_2 = 3.0$ mm, and $\sigma_f = 0.25$ mm, the true thickness $\tau_2 = 3.0$ mm is measured to be approximately 2.63 mm (−12.3% error). Figure 4(b) shows the measured thickness of a single sheet. In Fig. 4(b), the true thickness $\tau = 3.0$ mm is measured to be approximately 3.03 mm (1% error). Comparing Fig. 4(a) with Fig. 4(b), it can be seen that measured thickness of *Sheet*₂ is underestimated as comparison with that of a single sheet.

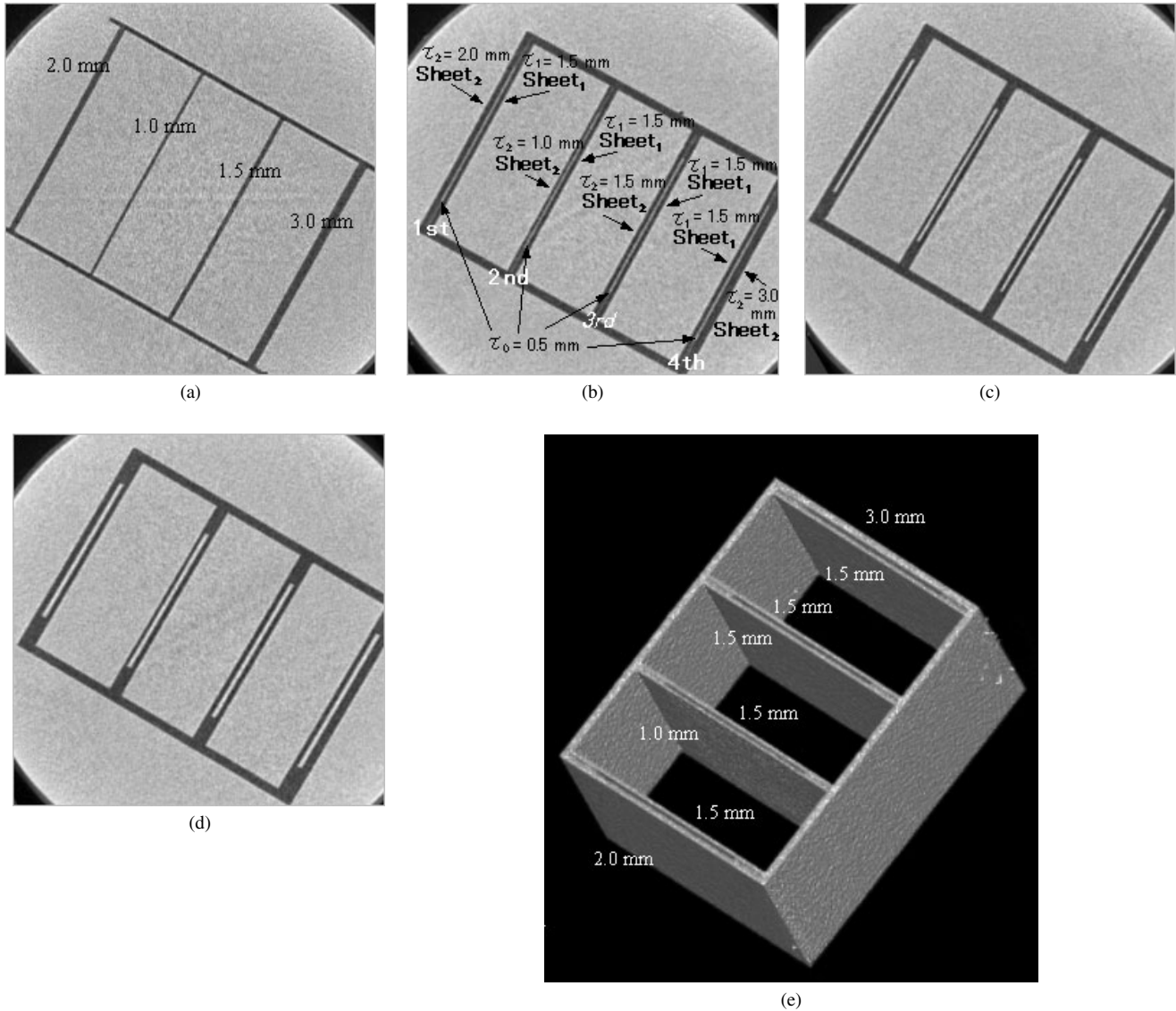


Fig.5 CT imaging of acrylic plate phantoms at an angle $\theta = 60^\circ$. The horizontal and vertical axes of the images correspond to the x axis and z axis, respectively. (a) CT imaging of phantom of single acrylic plate. The phantom consists of four single acrylic plates. Their thicknesses are shown in (a). (b) CT imaging of phantom of two adjacent acrylic plates with τ_0 (distance between *Sheet*₁ and *Sheet*₂) = 0.5 mm. Each phantom consists of four pairs of acrylic plates. *Sheet*₁ and *Sheet*₂ are placed parallel to each other, and their thicknesses are shown in (b). Phantom parameters with $\tau_0 = 0.5$ mm are given in Table 1 (a). (c) CT imaging of phantom of two adjacent acrylic plates with $\tau_0 = 1.0$ mm. Phantom parameters with $\tau_0 = 1.0$ mm are given in Table 1 (b). (d) CT imaging of phantom of two adjacent acrylic plates with $\tau_0 = 1.5$ mm. Phantom parameters with $\tau_0 = 1.5$ mm are given in Table 1 (c). (e) Volume rendering image of phantom with $\tau_0 = 0.5$ mm. A high opacity value was assigned to low CT values while zero opacity was assigned to high CT values.

2.4 Image Processing

2.4.1 Acrylic Plate Phantom

To test the proposed methods, four acrylic plate phantoms of sheet-like objects with known thickness were scanned. One was used for a single sheet; the other three were used for two adjacent sheets. The single sheet phantom was used to estimate the scanner PSF and to compare with the sheet structure influenced by the adjacent sheet structure.

The CT images were acquired using the Toshiba Aquilion CT scanner. Four phantoms were scanned with a slice width of 0.5 mm, 120 kV, 300 mA, 1 s at the four different tilt angles ($\theta = 0^\circ, 30^\circ, 60^\circ$ and 90° relative to the scan plane). The CT images were reconstructed with a field of view of 128 mm (256×256 matrix, pixel size = 0.5 mm). The phantom for the single sheet consisted of four acrylic plates of $80 \times 80 \text{ mm}^2$ with thickness of $\tau = 2.0, 1.0, 1.5,$ and 3.0 mm, placed parallel to each other (Fig.5 (a)). Each of the three phantoms for two adjacent sheets consisted of four pairs of acrylic plates, placed par-

Table 1 Phantom parameters for two adjacent sheets. Table shows $Sheet_1$ thickness (τ_1), $Sheet_2$ thickness (τ_2), and distance between $Sheet_1$ and $Sheet_2$ (τ_0).

(a) Distance between $Sheet_1$ and $Sheet_2$: $\tau_0 = 0.5$ mm.			
Sheet Number	τ_1	τ_0	τ_2
1	1.5 mm	0.5 mm	1.0 mm
2	1.5 mm	0.5 mm	1.5 mm
3	1.5 mm	0.5 mm	2.0 mm
4	1.5 mm	0.5 mm	3.0 mm

(b) Distance between $Sheet_1$ and $Sheet_2$: $\tau_0 = 1.0$ mm.			
Sheet Number	τ_1	τ_0	τ_2
1	1.5 mm	1.0 mm	1.0 mm
2	1.5 mm	1.0 mm	1.5 mm
3	1.5 mm	1.0 mm	2.0 mm
4	1.5 mm	1.0 mm	3.0 mm

(c) Distance between $Sheet_1$ and $Sheet_2$: $\tau_0 = 1.5$ mm.			
Sheet Number	τ_1	τ_0	τ_2
1	1.5 mm	1.5 mm	1.0 mm
2	1.5 mm	1.5 mm	1.5 mm
3	1.5 mm	1.5 mm	2.0 mm
4	1.5 mm	1.5 mm	3.0 mm

allel to each other (Fig. 5 (b)–(d)). One of their volume rendering images is shown in Fig. 5 (e). The parameters (τ_1 , τ_0 , and τ_2) of three phantoms are given in Table 1 (a) for $\tau_0 = 0.5$ mm, Table 1 (b) for $\tau_0 = 1.0$ mm, and Table 1 (c) for $\tau_0 = 1.5$ mm.

The phantoms were put in a contrast agent bath so that the background (contrast agent) showed higher intensity as contrasted to low intensity objects (acrylic plates) (Fig. 5). In order to match a predicted profile with an actual profile observed in the CT images of phantom, we performed the intensity transformation of CT images. Consequently, the objects (acrylic plates) showed higher intensity as contrasted to low intensity background (contrast agent).

2.4.2 Interpolation

In order to reduce the effects of discretization, the actual 3D images of phantoms are interpolated using sinc interpolation in the x , y , z directions so that the voxel interval became half of the original interval (0.5 mm). In this experiment, the voxel interval of the volume data $I(\vec{x})$ is $\Delta = 0.25$ mm.

2.4.3 Phantom Measurement Procedure Based on Zero-Crossings Method

In the real CT images of acrylic plate phantom, thickness measurement of $Sheet_2$ mainly includes the following two stages.

- i) Extraction of $Sheet_2$: In the actual images of phantoms,

it is necessary to extract the initial $Sheet_2$ regions before thickness determination. Using an automated segmentation technique [12], the approximated segmented regions of $Sheet_2$ are extracted.

- ii) Thickness determination: For the extracted 3D $Sheet_2$ regions, a procedure analogous to that described in [8] is employed to find the zero-crossings p and q for $Sheet_2$. The thickness of $Sheet_2$ is defined as the distance between p and q .

2.5 Parameter Estimation of CT Scanner PSF

We used CT images of the phantom with a single acrylic plate (Fig. 5 (a)) to estimate the PSF of the scanner. Let σ_{xy} ($= \sigma_x = \sigma_y$) be the x - y plane standard deviation. CT volume data of a single acrylic plate with a tilt angle of $\theta = 90^\circ$ is used to estimate the x - y plane standard deviation σ_{xy} and CT volume data with a tilt angle of $\theta = 0^\circ$ is used to estimate the standard deviation in the z direction (σ_z). A nonlinear optimization technique is used to match the gray-level profile of simulated scanner model with actual gray-level profile observed in CT data $I[\vec{x}]$ along \vec{r}_θ . The PSF estimation of the scanner procedure involves the following two stages.

Estimation of σ_{xy} : Let the observed profile be sampled at N discrete points in the actual image at a tilt angle of $\theta = 90^\circ$. Using the known thickness τ , σ_{xy} , L_t , and L_b are estimated by finding the values of σ_{xy} , L_t , and L_b minimizing

$$E(\sigma_{xy}, L_t, L_b) = \sum_{i=1}^N \{I(s_i) - f(s_i; \tau, \sigma_{xy}, L_t, L_b)\}^2. \quad (12)$$

where s_i is the i th sample along the sheet normal orientation in the actual image. L_t and L_b are the gray-levels of sheet structure and both sides of backgrounds for an ideal model of a single sheet structure. An optimization technique based on the Levenberg-Marquardt algorithm is used to solved this non-linear least square problem. The σ_{xy} is obtained as the average of all the results.

Estimation of σ_z : Let the observed profile be sampled at N discrete points in the actual image at a tilt angle of $\theta = 0^\circ$. Using the known thickness τ , σ_z , L_t , and L_b are estimated by finding the values of σ_z , L_t , and L_b minimizing

$$E(\sigma_z, L_t, L_b) = \sum_{i=1}^N \{I(s_i) - f(s_i; \tau, \sigma_z, L_t, L_b)\}^2. \quad (13)$$

where s_i is the i th sample along the sheet normal orientation in the actual image. An optimization technique based on the Levenberg-Marquardt algorithm is used to solved this non-linear least square problem. The σ_z is obtained as the average of all the results.

2.6 Proposed Method of Thickness Determination Based on the CT Imaging Model

As described in the previous section, zero-crossings method

can yield large measurement errors for two adjacent sheet structures. To correct the measurement errors, we propose a new measurement method based on a model of the scanning process. We model the scanning process of the ideal two adjacent sheets and use the model to predict the shape of gray-level profiles along the sheet normal direction given in Eq. (7). The difference between the predicted profile and the actual profile observed in the CT data is minimized by refining the model parameters. The set of parameters that minimizes the difference between model and the data yields the thickness estimation of the sheet structure.

We assume that H_t , H_0 , and H_b are constant, while τ_1 , τ_0 , and τ_2 are variable at the different locations in the hip joint. We use zero-crossings method for estimating τ_1 , τ_0 , and τ_2 . Because H_t , H_0 , and H_b are constant in the entire image, if we have found one location where measured values of τ_1 , τ_0 , and τ_2 are regarded as a good approximation of true values τ_1 , τ_0 , and τ_2 , H_t , H_0 , and H_b at this location can be estimated accurately using this accurately measured values of τ_1 , τ_0 , and τ_2 . In our case, when measured values of τ_1 , τ_0 , and τ_2 are 1.5 mm or above, these measured values can be regarded as a good approximation of their true values (This will be confirmed later in Figs. 7 and 8 of Sect. 3). If we might find several locations that satisfied the condition mentioned above, all H_t , H_0 , and H_b estimated at these locations are averaged, respectively, and these average values are regarded as the estimated values of H_t , H_0 , and H_b . Furthermore, τ_1 , τ_0 , and τ_2 at all locations are estimated accurately using H_t , H_0 , and H_b obtained above, since H_t , H_0 , and H_b are constant in the entire image. Briefly, the estimation procedure involves the following two steps: 1) the intensity heights of H_t , H_0 , and H_b are estimated with the accurately measured values of τ_1 , τ_0 , and τ_2 ; and 2) τ_1 , τ_0 , and τ_2 are estimated using H_t , H_0 , and H_b estimated in the first step.

2.6.1 Estimation of H_t , H_0 , and H_b

To estimate the density values of H_t , H_0 , and H_b , the gray-level profile observed in the actual data needs to be fit to the modeled profile. Using the model of the scanning process, we can obtain the 1D profile of the predicted gray level $f(s; \tau_1, \tau_0, \tau_2)$ (given in Eq. (7)) from $f(\vec{x}; \tau_1, \tau_0, \tau_2)$ along the sheet normal direction \vec{r}_θ . Similarly, 1D profile of the actual gray level $I(s)$ is derived from CT image $I(\vec{x})$ along \vec{r}_θ . The reconstruction of 1D profile $I(s)$ is performed at the sub-voxel resolution by using a trilinear interpolation.

Let T_1 , T_0 , and T_2 denote measured values of true values τ_1 , τ_0 , and τ_2 , respectively, as estimated by zero-crossings method. In our case, for $T_1 \geq 1.5$ mm, $T_0 \geq 1.5$ mm, and $T_2 \geq 1.5$ mm, these measured values are regarded as a good approximation of τ_1 , τ_0 , and τ_2 . Let the observed profile be sampled at N discrete points in the actual image. With T_1 , T_0 , and T_2 satisfied the condition $T_1 \geq 1.5$ mm, $T_0 \geq 1.5$ mm, and $T_2 \geq 1.5$ mm, H_t , H_0 , and H_b are estimated by finding the values of H_t , H_0 , and H_b minimizing

$$E(H_t, H_0, H_b) = \sum_{i=1}^N \{I(s_i) - f(s_i; T_1, T_0, T_2, H_t, H_0, H_b)\}^2. \quad (14)$$

where s_i is the i th sample along the sheet normal orientation in the actual image. An optimization technique based on the Levenberg-Marquardt algorithm is used to solve this non-linear least square problem. Initial estimations of model parameters are required to start the optimization process. The initial values for H_t , H_0 , and H_b are determined from the gray-level of CT image. We assume that H_t , H_0 , and H_b are not locally variable and thus those are obtained as averages of all the results from the sequences of the gray level profiles.

2.6.2 Estimation of τ_1 , τ_0 , and τ_2

Using estimated H_t , H_0 , and H_b in the first step, τ_1 , τ_0 , and τ_2 are searched minimizing

$$E(\tau_1, \tau_0, \tau_2) = \sum_{i=1}^N \{I(s_i) - f(s_i; \tau_1, \tau_0, \tau_2, H_t, H_0, H_b)\}^2. \quad (15)$$

In this step, we use two optimization methods to minimize Eq. (15).

- i) We use the one-by-one search (exhaustive combination search) method to minimize Eq. (15). The τ_1 and τ_0 are discretized from 0.2 to 12 voxels with 0.2 voxel fixed interval (voxel interval = 0.25 mm), respectively, and τ_2 is discretized from 0.2 to 24 voxels with 0.2 voxel fixed interval. For all the combinations of discretized model parameters τ_1 , τ_0 , and τ_2 , using the estimated H_t , H_0 , and H_b in the first step, the cost function $E(\tau_1, \tau_0, \tau_2)$ given in Eq. (15) is calculated. Among all the combinations of the model parameters τ_1 , τ_0 , and τ_2 , one combination of discretized model parameters τ_1 , τ_0 , and τ_2 corresponding to minimum value of cost function $E(\tau_1, \tau_0, \tau_2)$ is regarded as the estimations of τ_1 , τ_0 , and τ_2 . These estimations will be used as the initial estimations in the following optimization process.
- ii) We employ a nonlinear technique based on Levenberg-Marquardt algorithm to minimize Eq. (15). After iterative minimization, the model parameters τ_1 , τ_0 , and τ_2 yield the thickness estimations of sheet structures. Initial estimations of model parameters are required to start the optimization process. Levenberg-Marquardt algorithm can yield the considerable estimation biases when applying the zero-crossings method to obtain the initial values of τ_1 , τ_0 , and τ_2 . Thus, the one-by-one search method is used to obtain the initial estimations of τ_1 , τ_0 , and τ_2 .

3. Results

Figure 6 shows the actual gray-level profile and the model-

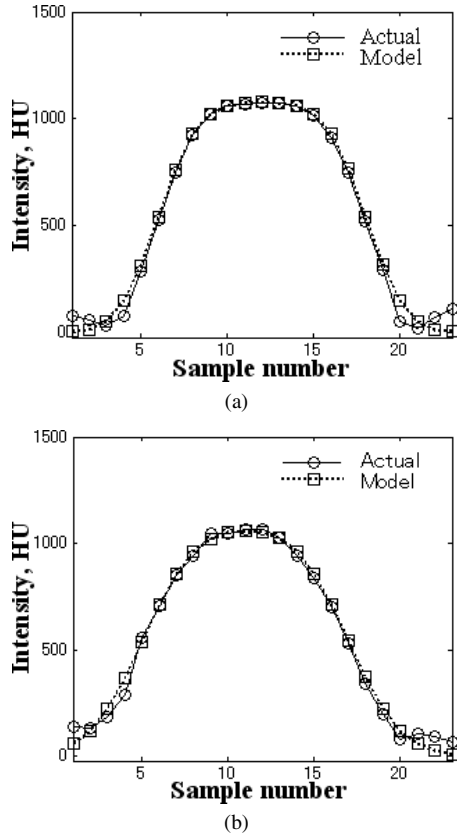


Fig. 6 Actual gray-level profile and modeled gray-level profile along the sheet normal direction after nonlinear optimization technique base on the Levenberg-Marquardt algorithm for estimating the scanner PSF. (a) Estimating the in-plane scanner PSF σ_{xy} . Using the phantom of single sheet with a thickness of $\tau = 3.0$ mm at an angle $\theta = 90^\circ$, the in-plane scanner PSF σ_{xy} was estimated to be approximately 0.453 mm. (b) Estimating the scanner PSF σ_z in the z direction. Using the phantom of single sheet with a thickness of $\tau = 3.0$ mm at an angle $\theta = 0^\circ$, the scanner PSF σ_z was estimated to be approximately 0.596 mm. In this experiment, the in-plane scanner PSF (σ_{xy}) was estimated to be approximately 0.45 ± 0.06 mm, and the scanner PSF in the z direction (σ_z) was estimated to be approximately 0.60 ± 0.08 mm. Graphs show the average and the SD of the estimated scanner PSF with 50 rays (along the sheet normal direction) used to form the measurement ($N = 50$).

predicted profile along the sheet normal after the nonlinear optimization technique based on the Levenberg-Marquardt algorithm for estimating the scanner PSF. Figure 6(a) shows the actual gray-level and the model-predicted profiles when the sheet structure is oriented obliquely to the scan plane at an angle of $\theta = 90^\circ$. The in-plane scanner PSF (σ_{xy}) was estimated to be approximately 0.45 ± 0.06 mm. Figure 6(b) shows the actual gray-level and the model-predicted profiles when the sheet structure is oriented obliquely to the scan plane at an angle of $\theta = 0^\circ$. The scanner PSF in the z direction (σ_z) was estimated to be approximately 0.60 ± 0.08 mm.

In Fig. 7, we compared the measured thickness of single sheet with that of *Sheet*₂ which is influenced by *Sheet*₁ by using zero-crossings method. Figure 7 shows the averages of the actually measured thickness obtained from CT imaging of acrylic phantom and the plots of the simulated

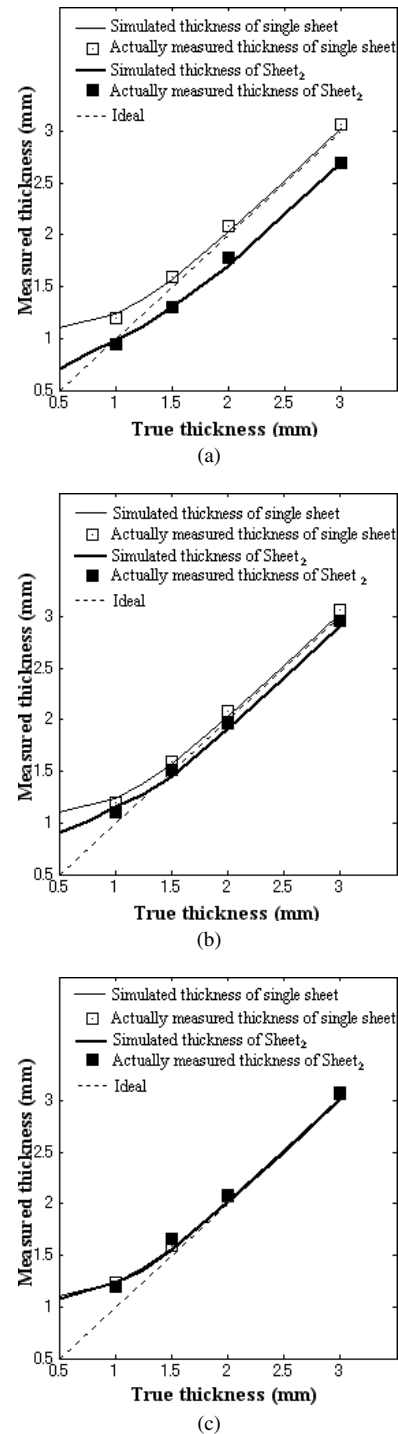


Fig. 7 Comparing the measured thickness of single sheet and *Sheet*₂ by using zero-crossings method. The scanner PSF: $\sigma_{xy} = 0.45$ and $\sigma_z = 0.60$; Gaussian filter width: $\sigma_f = 0.25$. The sheet structure is oriented obliquely to the scan plane at an angle $\theta = 90^\circ$. The biases between the simulated thickness and average of actually measured thickness were predominantly around 0.1 mm or less, and SDs (standard derivative) of actually measured thickness were mostly around 0.1 mm (not shown). Graphs show the average and the SD of actually measured thickness with 50 rays (along the sheet normal direction) used to form the measurement (Sample number: $N = 50$). (a) $\tau_0 = 0.5$ mm. (b) $\tau_0 = 1.0$ mm. (c) $\tau_0 = 1.5$ mm.

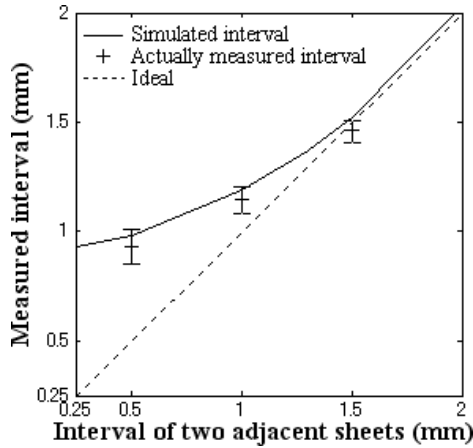


Fig. 8 Relationships between the true interval τ_0 and the measured interval T_0 . *Sheet*₁ thickness: $\tau_1 = 1.5$ mm; *Sheet*₂ thickness: $\tau_2 = 1.0$ mm. The scanner PSF: $\sigma_{xy} = 0.45$ and $\sigma_z = 0.60$; Gaussian filter width: $\sigma_f = 0.25$. Tilt angle: $\theta = 90^\circ$. Interval value between two sheets was measured by zero-crossings method. Graph shows for $T_0 \geq 1.5$ mm, these values approached to their true interval τ_0 .

thickness when the sheet structure is oriented obliquely to the scan plane at an angle of $\theta = 90^\circ$ for single sheet and *Sheet*₂. A good agreement between the simulated and the actually measured thickness was observed in Fig. 7. For a single sheet structure, thickness of thicker-structures was measured accurately: for instance, measurement of $\tau = 2.0$ mm yielded a result of 2.02 mm (0.02 mm or 1% overestimation); whereas thickness of thinner-structures was overestimated: for instance, measurement of $\tau = 1.0$ mm yielded a result of 1.25 mm (0.25 mm or 25% overestimation). For two adjacent sheet structures, in the case of $\tau_0 = 0.5$ mm (Fig. 7 (a)), compared with the measured thickness of single sheet, thickness of *Sheet*₂ was underestimated by approximately 0.3–0.35 mm. Also, compared with its true thickness, measured thickness was underestimated for thicker-structure: for instance, $\tau_2 = 2.0$ mm and 3.0 mm were measured by 1.70 mm (0.30 mm or 15% underestimation) and 2.69 mm (0.31 mm or 10.3% underestimation), respectively; whereas measured thickness was overestimated for thinner-structure: for instance, $\tau_2 = 0.5$ mm was measured by 0.7 mm (0.20 mm or 40% overestimation), respectively. In the case of $\tau_0 = 1.0$ mm. (Fig. 7 (b)), measured thickness of *Sheet*₂ was also less than that of single sheet. Also, compared with its true thickness, its thickness was slightly underestimated for thicker-structure, whereas its thickness was overestimated for thinner-structure. In the case of $\tau_0 = 1.5$ mm (Fig. 7 (c)), measured thickness of *Sheet*₂ was approximately equivalent to that of single sheet. For the true thickness $\tau_2 \geq 1.5$ mm, its thickness can be accurately measured: for instance, thickness of $\tau_2 = 1.5$ was measured by 1.55 mm (0.05 mm or 3.33% error). In addition, we performed the above measurements for $\theta = 0^\circ$, $\theta = 30^\circ$, and $\theta = 60^\circ$, respectively. These results were the same trend as exhibited by results at $\theta = 90^\circ$.

In Fig. 8, with $\tau_1 = 1.5$ mm and $\tau_2 = 1.0$ mm, interval

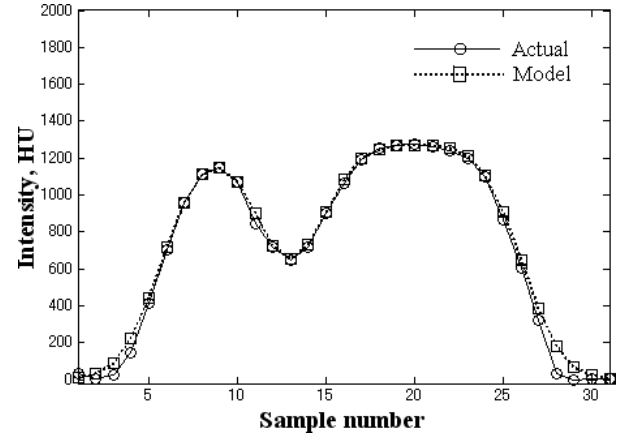


Fig. 9 Actual gray-level profile and modeled gray-level profile along the sheet normal direction after nonlinear optimization technique base on the Levenberg-Marquardt algorithm for estimating the thickness of *Sheet*₂. The scanner PSF: $\sigma_{xy} = 0.45$ and $\sigma_z = 0.60$. The actual image of acrylic plate phantom at $\theta = 60^\circ$ was used, and actual phantom parameters (*Sheet*₁ thickness: $\tau_1 = 1.5$ mm, *Sheet*₂ thickness: $\tau_2 = 3.0$ mm, distance between them: $\tau_0 = 0.5$ mm) are given in Table 1 (a). For the Levenberg-Marquardt algorithm, initial estimations of the model parameters are required to start the optimization process. One-by-one search method is used to obtain the initial estimations of τ_1 , τ_0 , and τ_2 . Zero-crossing method: $\tau_2 = 3.0$ mm was estimated to be approximately 2.67 mm (–11% error); One-by-one search method: $\tau_2 = 3.0$ mm was estimated to be approximately 3.11 mm (3.67% error); Levenberg-Marquardt method: $\tau_2 = 3.0$ mm was estimated to be approximately 3.05 mm (1.67% error).

between two sheets was measured by using zero-crossings method. A good agreement between the simulated and the actually measured intervals was shown in Fig. 8. The results of Fig. 8 show that for the true interval $\tau_0 \geq 1.5$ mm, measured interval value T_0 is approximately equivalent to the true interval τ_0 . From the results of Figs. 7 and 8, it can be seen that when using zero-crossings method, in our case, for T_2 (measured value of $\tau_2 \geq 1.5$ mm and $T_0 \geq 1.5$ mm, these measured values approached to their true values. Similarly, with $\tau_1 = 1.5$ mm and $\tau_2 = 1.5, 2.0$, and 3.0 mm, respectively, comparisons between τ_0 and T_0 were performed, respectively. The same results as Fig. 8 were observed. Also, for T_1 (measured value of $\tau_1 \geq 1.5$ mm, these measure values should be accurate.

Figure 9 shows the actual gray-level profile and the modeled gray-level profile along the sheet normal direction after the nonlinear optimization technique based on the Levenberg-Marquardt algorithm for estimating the thickness of *Sheet*₂ at a tilt angle of $\theta = 60^\circ$. The phantom with $\tau_1 = 1.5$ mm, $\tau_0 = 0.5$ mm, and $\tau_2 = 3.0$ mm was used. The zero-crossings method yielded a result of 2.67 mm (–11% error) for $\tau_2 = 3.0$ mm. One-by-one search method yielded the results of 1.62 mm for $\tau_1 = 1.5$ mm, 0.67 mm for $\tau_0 = 0.5$ mm, and 3.11 mm (3.67% error) for $\tau_2 = 3.0$ mm. Using the initial values of $\tau_1 = 1.62$ mm, $\tau_0 = 0.67$ mm, and $\tau_2 = 3.11$ mm estimated by one-by-one search method, Levenberg-Marquardt method yielded the results of 1.56 mm for $\tau_1 = 1.5$ mm, 0.58 mm for $\tau_0 = 0.5$ mm, and 3.05 mm (1.67% error) for $\tau_2 = 3.0$ mm. Thus, Levenberg-

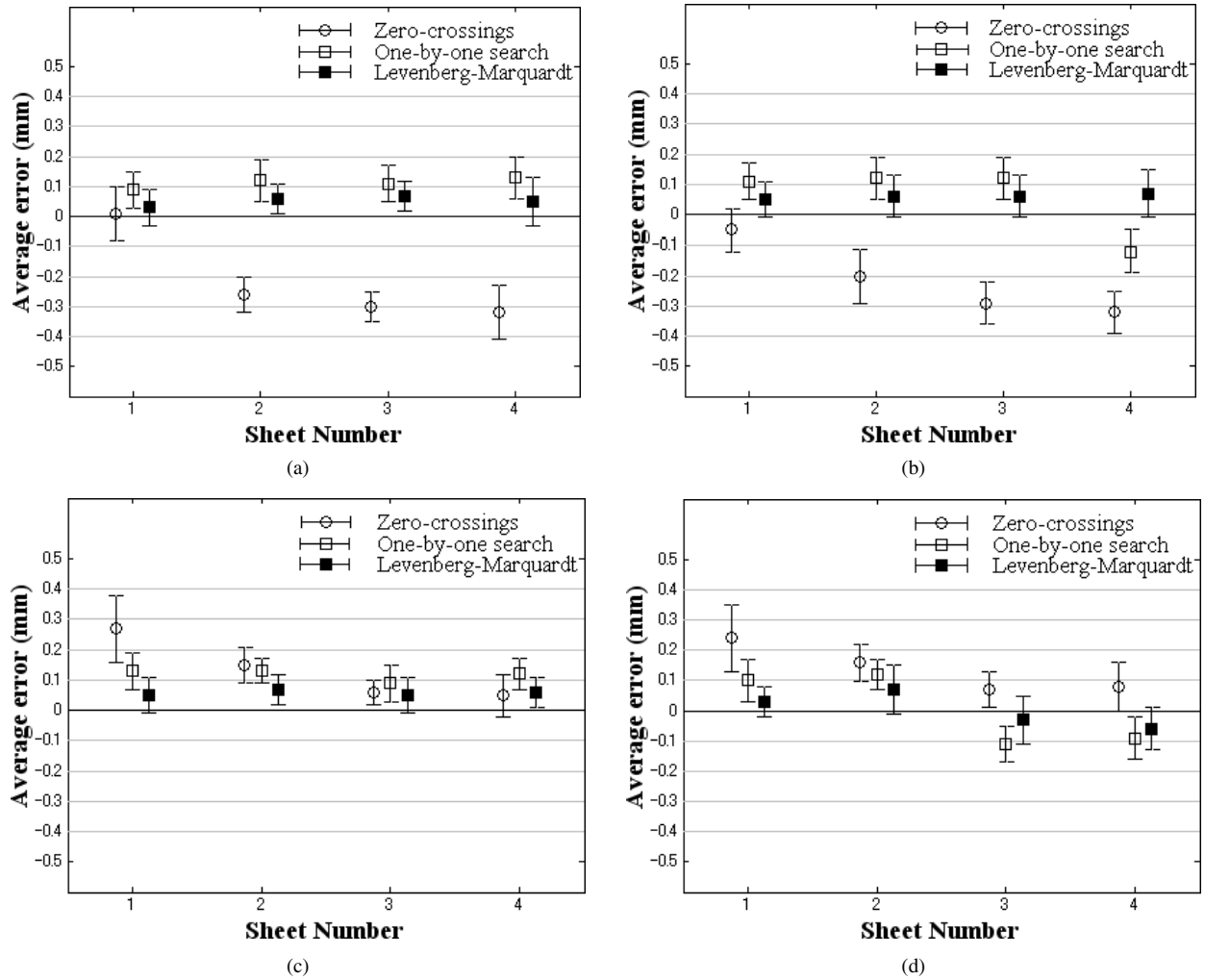


Fig. 10 Comparing the performance of three methods (zero-crossing, one-by-one search, and Levenberg-Marquardt) for estimating the thickness of *Sheet*₂. Graphs show the average measurement error and the SD of the measurement error with 50 rays (along the sheet normal direction) used to form the measurement (Sample number: $N = 50$). The measurement error is defined as $E = T_2 - \tau_2$. (a) The tilt angle $\theta = 0^\circ$; Distance between *Sheet*₁ and *Sheet*₂: $\tau_0 = 0.5$ mm. (b) $\theta = 60^\circ$; $\tau_0 = 0.5$ mm. (c) $\theta = 0^\circ$; $\tau_0 = 1.5$ mm. (d) $\theta = 60^\circ$; $\tau_0 = 1.5$ mm. For (a) and (b), phantom parameters are given in Table 1 (a); for (c) and (d), phantom parameters are given in Table 1 (c). In the figures, sheets 1, 2, 3, and 4 correspond to 1.0, 1.5, 2.0, and 3.0 mm, respectively, with respect to the thickness of *Sheet*₂.

Marquardt method was more accurate for this case.

Figure 10 shows the average measurement error and the SDs of the measurement error for the zero-crossings, one-by-one search, and Levenberg-Marquardt methods. As shown in Figs. 10(a) and (b), in the case of $\tau_0 = 0.5$ mm, the measured thickness of *Sheet*₂ was influenced by *Sheet*₁ when using zero-crossings method. The initial values of τ_1 , τ_0 , and τ_2 was estimated by one-by-one search method for using Levenberg-Marquardt method. Levenberg-Marquardt method gave measurements with less estimation bias than zero-crossings and one-by-one search methods. As Figs. 10(c) and (d) illustrated, in the case of $\tau_0 = 1.5$ mm, the measured thickness of *Sheet*₂ was not influenced by *Sheet*₁ when using zero-crossings method. Comparing the performance of three methods, Levenberg-Marquardt method was more accurate than the others.

4. Discussion

The theoretical simulation and phantom measurements show that when two sheet structures are close to each other, a conventional measurement technique, zero-crossings method, yields considerable measurement biases (Fig. 7). This is caused by the finite resolution of imaging scanners [14] and blurring involved in edge detector.

Note that the influence between *Sheet*₁ and *Sheet*₂ was dependent on the distance τ_0 between *Sheet*₁ and *Sheet*₂. As the distance τ_0 decreases, the error in measuring the thickness of sheet structures increases. When the distance τ_0 reaches to a certain value, two sheet structures can no longer influence each other. This value can be predicted by using our simulation method. In our present work, when the

distance τ_0 was 1.5 mm, the measured thickness of *Sheet₂* was approximately equivalent to that of the single sheet (Fig. 7(c)). We may regard *Sheet₂* as a single sheet structure when the distance $\tau_0 = 1.5$ mm. It should be noted that the value of τ_0 at which the influence is negligible depends on degrees of both the scanner PSF and the blurring involved in edge detectors. The results of Fig. 7(c) show that when using the zero-crossings method, thickness of thinner-structure is overestimated, whereas thickness of thicker-structure is accurately measured. This is consistent with our results of the previous study [8]–[10] for thickness measurement of a single sheet structure.

From the experimental results of Figs. 7 and 8 it can be deduced that when using zero-crossings method, for $T_1 \geq 1.5$ mm, $T_2 \geq 1.5$ mm, and $T_0 \geq 1.5$ mm, these values can be regarded as a good approximation of true values τ_1 , τ_2 , and τ_0 . It should be noted that our proposed method includes two steps described in Sect. 2.6. In the first step, we use zero-crossings method for estimating τ_1 , τ_2 , and τ_0 . We should find at least one location where measured values of τ_1 , τ_2 , and τ_0 are 1.5 mm or above. Furthermore, using this accurately measured values of τ_1 , τ_2 , and τ_0 , H_t , H_0 , and H_b at this location can be estimated accurately. In the second step, τ_1 , τ_2 , and τ_0 at all locations can be estimated accurately with H_t , H_0 , and H_b obtained above, since H_t , H_0 , and H_b are constant in the entire image. On the other hand, in the first step, if we cannot find any location where measured values of τ_1 , τ_2 , and τ_0 are 1.5 mm or above when applying zero-crossings method, H_t , H_0 , and H_b cannot be estimated accurately. Then, in the second step, it is impossible to accurately estimate parameters τ_1 , τ_2 , and τ_0 . For this reason, we observed the real patient CT data sets. Consequently, finding some locations where measured values of τ_1 , τ_2 , and τ_0 are 1.5 mm or above should be possible.

In this work, an optimization technique based on Levenberg-Marquardt algorithm is used to minimize the difference between the predicted and the actual gray-level profiles observed in the CT data by refining the model parameters. One drawback for Levenberg-Marquardt algorithm is the fact that the initial values of the model parameters are required to start the optimization process, and using the poor initial values can give rise to large estimation biases. The zero-crossings method exhibited considerable estimation biases for the single sheet structure with small thickness and the two adjacent sheet structures (Fig. 7). An attempt was made to obtain the initial values of τ_1 , τ_0 , and τ_2 using zero-crossings method. Levenberg-Marquardt algorithm yielded the poor estimations of τ_1 , τ_0 , and τ_2 when applying the zero-crossings method to obtain the initial values. Thus, one-by-one search method was used to find the initial values of τ_1 , τ_0 , and τ_2 . Levenberg-Marquardt algorithm gave an accurate thickness measurement (Fig. 10).

In this study, the sheet plane angle was known. In the real clinical application, however, it is necessary to estimate the normal direction of the sheet structure. The estimation of normal direction of cartilage surface has been presented in [14] and [15]. In the healthy hip joint, the shape of the

femoral head approximates the exact sphere; therefore, the radial directions from the automatically detected center of the femoral head can be regarded as the normal direction of the cartilage surface [14]. However, as in the case of diseased hip joint, because the shape of the femoral head is not perfectly spherical, the method presented in [14] cannot be used. In such cases, the normal direction might be estimated using the eigenvectors of the Hessian matrix [15]. Our previous study demonstrated the effectiveness for the estimation of normal direction of sheet structure [14], [15].

In the hip joint, both the femoral head and the acetabulum are covered with cartilage. The ball and socket constitution of the hip joint, with strong capsule and ligaments, does not permit discrimination of the articular cartilage of the femoral head from the acetabulum. Both cartilages were separately depicted using a traction device for distending the joint space [16], and the contrast agents were used for enhancing the CT images. However, in many cases, the joint space between the femoral cartilage and acetabular cartilage is narrow despite traction. Therefore, it should be considered that two cartilages maybe influence each other on measurement accuracy of articular cartilage thickness when applying the zero-crossing method.

5. Conclusion

We model the CT imaging processes of two parallel sheet structures separated by a small distance and use this model to predict the shape of the gray level profiles along the normal orientation of the sheet surface. Using this model, we show that when applying zero-crossings method for measuring thickness of two adjacent sheets, in the case of measured interval $T_0 < 1.5$ mm, zero-crossings method can introduce considerable measurement biases. To correct the measurement error, a new approach based on the model of scanning process is presented to estimate the thickness of two adjacent sheet structures. The proposed approach estimates the thickness of sheet structures by matching a predicted profile with an actual profile observed in the CT data set. Both a one-by-one search (exhaustive combination search) technique and a nonlinear optimization technique based on the Levenberg-Marquardt technique are used to adjust the model parameters and to estimate the thickness of sheet structures. Experimental results show that when applying the one-by-one search technique to obtain the initial values of the model parameters, Levenberg-Marquardt algorithm can accurately estimate the thickness of two adjacent sheet structures, as well as the thickness of a single sheet structure. Therefore, using our proposed method, the accurate measurement of articular cartilages in the hip joint should be possible. Finally, our future work will focus on clinical validation using the patient CT data sets for clinical applications.

References

- [1] F. Eckstein, A. Gavazzeni, H. Sittke, M. Haubner, A. Loesch, S.

- Milz, K.H. Englmeier, E. Schulte, R. Putz, and M. Reiser, "Determination of knee joint cartilage thickness using three-dimensional magnetic resonance chondro-crassmetry (3D MR CCM)," *Magn. Reson. Med.*, vol.36, pp.256–265, 1996.
- [2] A.A. Kshirsagar, P.J. Watson, J.A. Tyler, and L.D. Hall, "Measurement of localized cartilage volume and thickness of human knee joints by computer analysis of three-dimensional magnetic resonance method," *Invest. Radiol.*, vol.33, pp.289–299, 1998.
- [3] J.P. Raynauld, C. Kauffman, G. Beaudoin, M.J. Berthiaume, J.A. de Guise, D.A. Bloch, F. Camacho, B. Godbout, R.D. Altman, M. Hochberg, J.M. Meyer, G. Cline, J.P. Pelletier, and J. Martel-Pelletier, "Reliability of a quantification imaging system using magnetic resonance images to measure cartilage thickness and volume in human normal and osteoarthritic knees," *Osteoarthritis Cartilage*, vol.11, pp.475–482, 2003.
- [4] J.S. Wayne, C.W. Brodrick, and N. Mukherjee, "Measurement of articular cartilage thickness in the articulated knee," *Ann. Biomed. Eng.*, vol.26, pp.96–102, 1998.
- [5] C.A. McGibbon, J. Bencardino, E.D. Yeh, and W.E. Palmer, "Accuracy of cartilage and subchondral bone spatial thickness distribution from MRI," *J. Magn. Reson. Imaging*, vol.17, pp.703–715, 2003.
- [6] K. Nakanishi, H. Tanaka, N. Sugano, Y. Sato, T. Ueguchi, T. Kubota, S. Tamura, and H. Nakamura, "MR-based three-dimensional presentation of cartilage thickness in the femoral head," *Eur. Radiol.*, vol.11, pp.2178–2183, 2000.
- [7] T. Nishii, N. Sugano, Y. Sato, H. Tanaka, H. Miki, and H. Yoshikawa, "Three-dimensional distribution of acetabular cartilage thickness in patients with hip dysplasia: A fully automated computational analysis of MR imaging," *Osteoarthritis Cartilage*, vol.12, pp.650–657, 2004.
- [8] Y. Sato, H. Tanaka, T. Nishii, K. Nakanishi, N. Sugano, T. Kubota, H. Nakamura, H. Yoshikawa, T. Ochi, and S. Tamura, "Limits on the accuracy of 3-D thickness measurement in magnetic resonance images-effects of voxel anisotropy," *IEEE Trans. Med. Imaging*, vol.22, no.9, pp.1076–1088, 2003.
- [9] S. Prevrhal, J.C. Fox, J.A. Shepherd, and H.K. Genant, "Accuracy of CT-based thickness measurement of thin structures: Modeling of limited spatial resolution in all three dimensions," *Med. Phys.*, vol.30, pp.1–8, 2003.
- [10] J.M. Reinhardt, N.D. D'Souza, and E.A. Hoffman, "Accurate measurement of intrathoracic airways," *IEEE Trans. Med. Imaging*, vol.16, no.6, pp.820–827, 1997.
- [11] G. Wang, M.W. Skinner, and M.W. Vannier, "Temporal bone volumetric image deblurring in spiral computed tomography scanning," *Acad. Radiol.*, vol.2, pp.888–895, 1995.
- [12] Y. Sato, C.F. Westin, A. Bhalerao, S. Nakajima, N. Shiraga, S. Tamura, and R. Kikinis, "Tissue classification based on 3-D local intensity structures for volume rendering," *IEEE Trans. Vis. Comput. Graphics*, vol.6, no.2, pp.160–180, 2000.
- [13] R.M. Hoogeveen, C.J.G. Bakker, and M.A. Viergever, "Limits to the accuracy of vessel diameter measurement in MR angiography," *JMRI-J. Magn. Reson. Imaging*, vol.8, pp.1228–1235, 1998.
- [14] Y. Sato, K. Nakanishi, H. Tanaka, N. Sugano, T. Nishii, H. Nakamura, T. Ochi, and S. Tamura, "A fully automated method for segmentation and thickness determination of hip joint cartilage from 3D MR data," *Proc. CARS 2001, International Congress Series 1230*, pp.352–358, 2001.
- [15] Y. Sato and S. Tamura, "Detection and quantification of line and sheet structures in 3-D images," *Proc. MICCAI 2000, Lecture Notes in Computer Science*, vol.1935, pp.154–165, 2000.
- [16] N. Nakanishi, H. Tanaka, T. Nishii, K. Masuhara, Y. Narumi, and H. Nakamura, "MR evaluation of the articular cartilage of the femoral head during traction," *Acta Radiol.*, vol.40, pp.60–63, 1999.



Yuanzhi Cheng entered into Graduate School of Mechatronics Engineering at Harbin Institute of Technology in 2002. He is currently completing the Ph.D in Harbin Institute of Technology Graduate School of Mechatronics Engineering and Osaka University Graduate School of Medicine.



Yoshinobu Sato was born in Kobe, Japan, in 1960. He received the B.S., M.S., and Ph.D. degrees in information and computer sciences from Osaka University, Japan, in 1982, 1984, 1988, respectively. From 1988 to 1992, he was a Research Engineer at the NTT Human Interface Laboratories. In 1992, he joined the Division of Functional Diagnostic Imaging, Osaka University Medical School, as a Faculty Member. From 1996 to 1997, he was a Research Fellow in the Surgical Planning Laboratory, Harvard Medical School and Brigham and Women's Hospital. He is currently an Associate Professor at Osaka University Graduate School of Medicine and an Adjunct Associate Professor with Graduate School of Information Science and Technology, Osaka University, where he leads a group conducting research on medical image analysis and computer-assisted surgery in the Division of Image Analysis (formerly, Functional Diagnostic Imaging).



Hisashi Tanaka was born in 1961. He received the M.D. degree from Osaka University Medical School, Osaka, Japan. He is currently a Lecturer in the Graduate School of Medicine, Osaka University. He is a member of the International Society for Magnetic Resonance in the Medicine and Radiological Society of North America.



Takashi Nishii was born in 1963. He received the M.D. and Ph.D. degrees from Osaka University Medical School, Osaka, Japan. He was a Research Assistant with Osaka University Graduate School of Medicine. Dr. Nishii is a Member of the International Society for Magnetic Resonance in the Medicine Orthopaedic Research Society.



Nobuhiko Sugano was born in 1960. He received the M.D. and Ph.D. degrees from Osaka University Medical School, Osaka, Japan, in 1985 and 1994, respectively. From 1994 to 1995, he was an Assistant Professor in the Department of Orthopaedic Surgery, Osaka University Medical School. From 1996 to 1997, he was an Assistant Professor in the Department of Orthopedic Surgery, Baylor College of Medicine, Houston, TX. In 1997, he returned to the Department of Orthopaedic Surgery at

Osaka University Medical School. He is currently an Assistant Professor (Lecturer) in Osaka University Graduate School of Medicine. His specialties are total joint arthroplasty and computer assisted orthopaedic surgery. Dr. Sugano is a Member of Orthopaedic Research Society, the Association of American Hip and Knee Surgeons, and the International Society of Computer Aided Surgery.



Shinichi Tamura received the B.S., M.S., and Ph.D. degrees in electrical engineering from Osaka University, Osaka, Japan, in 1966, 1968, and 1971, respectively. He is currently a Professor in the Graduate School of Medicine, Graduate School of Information Science and Technology, and the Center for Advanced Medical Engineering and Informatics, Osaka University. He has published more than 250 papers in scientific journals and received several awards from journals including Pattern Recognition and In-

vestigative Radiology. His current research activities include works in the field of medical image analysis and its applications. Currently he is a Editorial Board member of International Journal of Computer Assisted Radiology and Surgery. Dr. Tamura is a member of the Institute of Electronics, Information and Communication Engineers of Japan, the Information Processing Society of Japan, the Japanese Society of Medical Imaging Technology, and the Japan Radiological Society.



Hironobu Nakamura was born in 1946. He received the M.D. and Ph.D. degrees from Osaka University Medical School, Osaka, Japan. Currently he is a Professor and Chairman in Department of Radiology, Osaka University Graduate School of Medicine. He is elected as the President of Japan Radiological Society Meeting in 2007.



Hideki Yoshikawa was born in Japan on September 5, 1954. He received the M.D. and Ph.D. degrees from Osaka University Medical School, Osaka, Japan, in 1979 and 1983, respectively. Since 1999, he has been a Professor and Chairman of the Department of Orthopaedic Surgery, Osaka University Graduate School of Medicine.



Shuguo Wang now assumes the President of Harbin Institute of Technology. He received the B.S. Degree, the M.S. Degree, and the Ph.D. Degree in Mechatronics from the Harbin Institute of Technology, Harbin, China. He has assumed the position of Professor in the School of Mechatronics Engineering at the Harbin Institute of Technology since 1992. He has published more than 100 papers in scientific journals. During 1992–2000, Professor Wang served as Chief expert in Automation at the National High Technology Research and Development Program (863 Program), which was launched in March 1986 with the aim of enhancing China's international competitiveness and improving China's overall capability of R&D in high technology. Prof. Wang served as the chair/co-chair on the many national and International Robotics conference and also served on the National Science Foundation's Robotics Council from 1998–2005. In 1995, he received the Outstanding Senior Faculty Research Award from the Ministry of Education of China. He is a Senior Member of Chinese Mechanical Engineering Society.

ational High Technology Research and Development Program (863 Program), which was launched in March 1986 with the aim of enhancing China's international competitiveness and improving China's overall capability of R&D in high technology. Prof. Wang served as the chair/co-chair on the many national and International Robotics conference and also served on the National Science Foundation's Robotics Council from 1998–2005. In 1995, he received the Outstanding Senior Faculty Research Award from the Ministry of Education of China. He is a Senior Member of Chinese Mechanical Engineering Society.